J. Condensed Matter Nucl. Sci. 6 (2012) 149–168

Research Article

LANR Nanostructures and Metamaterials Driven at their Optimal Operating Point

Mitchell R. Swartz *

JET Energy Inc. Wellesley, MA, USA

Abstract

In lattice-assisted nuclear reactions (LANR, or LENR), the size and structural metamaterial shape of Pd–D nanostructures, and the deuterium flux through them all play decisive roles. The spiral Phusor®-type cathode system with open helical cylindrical geometry in a high electrical resistance solution is a LANR metamaterial design creating an unusual electric field distribution and requisite intrapalladial deuteron flow. Optimal operating point (OOP) technology allows improved and more reproducible operation. LANR power gain can be considerable. In situ imaging has revealed that the excess power gain is linked to non-thermal near-IR emission when the LANR devices are operated at their OOP.

Keywords: Deuterium, Lattice-assisted nuclear reactions, Loading flux, Metamaterials, Nanostructures, OOP manifolds, Optimal operating point, Palladium

1. Impact of Nanostructure, Size and Shape

Lattice assisted nuclear reactions (LANR) use hydrogen-loaded alloys to enable near room temperature deuterium fusion and other nuclear reactions [1–49] and nanostructures, metamaterials, and controlled operation are required for success. This paper will review the astounding range of LANR nanostructures is observed, including some generated within palladium and others created on its surface. Such Pd–D nanostructures are needed for successful LANR generated excess heat (XSH). Table 1 lists the LANR nanostructure issues covered in this paper and their impact on LANR.

LANR's generated excess heat is a response to relatively low energy initiation to produce excess power densities ranging from ~ 7 (1989 announcement) to 80–10,000 W/cm^3, today. This magnitude of excess energy, in the absence of sufficient thermal relaxation times, yields significant heat and even changes which are wrought upon the electrode as volcano-like pits [8,18,19]. At LANR's "core" are deuterons which are tightly packed into binary ("highly loaded") metals and metallic nanostructures by an applied electric field or elevated gas pressure which supply deuterons in heavy water or gaseous deuterium.

*E-mail: mica@theworld.com

Table 1. LANR structure, shape, and priming for LANR Success

Size of nanostructure	Increased XSH if $>\sim 7$ nm
Purity of LANR structure	LANR quenched by contamination
Control of deuterium flow	Requisite for, and increases, XSH
Metamaterial shape	4–14 dB power gain in XSH
OOP control	8–25 dB power gain in XSH
Near IR emission at OOP	Confirmation of XSH
Multisystem calorimetry	Confirmation of XSH

Proof that nanostructures are important in LANR include codeposition, the diversity of LANR structure (Section 2), and non-thermal near IR emissions [25,34], and other recent data, such as shown in Fig. 1. The curve in Fig. 1 might be some of the first experimental evidence that LANR excess heat is correlated with the size of the Pd–D nanostructures. It shows a monotonic increase in excess heat from LANR as the codepositional layer was increased in size.

These relevant LANR nanostructures are discussed regarding the local and regional structure in Sections 3 and 4. The methods of driving LANR are discussed in Sections 5 and 6, both theoretically and experimentally, and some of the results are shown in Section 4. High impedance metamaterial nanostructured LANR devices have shown power gains more than 200% and short term power gains to $\sim$ 8000% [1,2], compared to input energy and to input energy transferred to conventional dissipative devices. The excess energies observed with LANR are greater than any known chemical reaction. They are also increasingly studied. By the end of this chapter, the reader should understand the breadth of Pd–D nanostructures, how the nanostructure size correlates to the 'excess heat' observed in successful LANR systems (Fig. 1), and how the additional LANR operating condition requirements can be satisfied using metamaterials (Fig. 3) and the secondary deuterium flux (Fig. 4), in combination with optimum operating point driving (Fig. 5).

2. Lanr Nanostructure Diversity

The nanostructures arise, in part, because of the unique complex behavior of palladium and its binary alloy with hydrogen. It will be demonstrated in this section that LANR reactions are generated in one of three types of sites within, or upon, the deuteron-loaded, palladium ([50,51], Fig. 2). Each location has its own, characteristic production

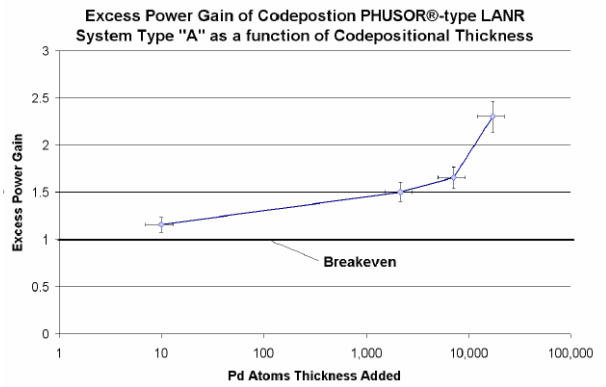

Figure 1. Excess heat in LANR is correlated with palladium codeposition thickness

rate of excess heat, tritium, and helium, each characterized by a different optimal operating point (OOP) manifold [52–57], and they are both heterogeneous and diverse. This occurs because palladium is a unique metal [50,51,58,59] with one-of-a-kind properties. Many of them involve the incredible solubility of D and H in Pd. The binary alloy, hydrogen–palladium, is perhaps the most studied hydrogen system. Two solid solutions exist under normal conditions. The lattice parameter increases with hydrogen content, increasing from 3.891Å for pure Pd to 3.902Å for the saturated alpha phase. In some crystals, the Pd^{2+} ion occurs, such as in PdF_2, and is paramagnetic. But, in aqueous solution, the $[Pd(H_2O)_4]^{2+}$ diamagnetic ions [60] form complexes ("chelates") which are square or 5-coordinate.

Relevant to LANR, palladium nanostructures include nanoparticles, nanowires, nanocrystals, nanoclusters, dendrimers, higher polymer aggregates, organic Pd hybrids, vacancy state materials, and many types of shaped alloys. They usually range in size from 2 to 200 nm. Palladium nanoparticles and nanowires are created by electrochemical deposition, usually on a carbon surface. They often have a vacancy in their center [61]. Similarly, LANR nanostructures include vacancies within them. In the alloys, they must drift into the bulk from the surface. This diffusion is slightly facilitated by the loading itself [1,2]. Swartz and Hagelstein have made Pd–D vacancies with electron beam irradiation [62]. Jan Marwan has improved the field by generating new methods of making additional "vacancies" with nanolipids and dyes [63].

Pd nanoparticles made on a gold surface show proton reduction catalytic activity enhanced by more than two orders of magnitude, as the diameter of the palladium particles decreases from 200 to 6 nm [64]. Pd nanoparticles can be made by poly(ethyleneglycol) (PEG) and $Pd(OAc)_2$, where PEG is both reducing agent and stabilizer. The reduction of Pd^{2+} to nano Pd is sensitive to the chain length of the PEG, with larger chain lengths improving performance [65]. Larger spherical Pd nanoparticles, ∼70 nm, are made with palladium acetate and octa(3-aminopropyl)octasilsesquioxane octahydrochloride [66].

Wire-shaped Pd nanoparticles, 5 nm in diameter and 1000 nm long are synthesized using poly(methacryloyloxyethyl dimethylbenzylammonium chloride and Si-wafers [67]. Colloidal Ni/Pd nanoclusters are made using ethylene glycol and *N*-vinyl-2- pyrrolidone with a molar ratio of Ni : Pd = 2 : 3. They exhibit 3.5 times greater activity than typical colloidal palladium catalysts [68]. Nanocrystalline palladium has been made by inert gas condensation and compaction with grain, crystallite, sizes ranging from 5 to 50 nm [69]. Palladium nanodendrimers of ∼ 300 Pd atoms in a metallic core of 2.0 nm diameter are also fabricated [70]. Nearly 90% of the metal nanoparticle surface is unpassivated and available for catalysis. The dendrons inhibit metal agglomeration without adversely affecting chemical reactivity [71].

Some dynamically formed Pd D nanostructures in LANR are even more complicated. The nature of activation and energy transfer processes in LANR are debated, but the diversity of LANR sites of varying sizes and locations are not. A variety of LANR regions are involved upon -and within- the deuteron-loaded Pd lattice. Figure 2 shows some of these diverse LANR sites - which include the deep and superficial lattice, and above-surface structures generated during codeposition. Three different physical locations [material types] are distinguished [50,51]. Each location has distinctive rates of excess heat, and tritium and helium product generation, each controlled by a different OOP manifold. Each location is a compartment of LANR active sites which can be distinguished by calorimetry and spectroscopy, including by near infrared (IR) emission [34].

Experimental evidence for (at least) three different LANR regions include the two types of time constants associated with "heat after death" (HAD) and the monotonic increase of excess heat observed in LANR systems with increase of loaded depth. Region 1 refers to the most superficial portions of the palladium, including surface dendrites and a variety of micro- and nanoparticles, that characterize electrodeposits by codeposition. This involves at least several atomic layers. These surface sites, generated via codeposition and conventional LANR produce tritium. At the top left,

Figure 1 shows supra-surface palladium surface globules (Image A) produced during palladium codeposition upon a copper cathode at SPAWAR [19,20]. Codeposition efforts, including these at SPAWAR, produce subsurface reactions, involving at least several atomic layers. Palladium rods are shown which develop from the globules (Image B), produced after additional applied electric field; one of several morphologies generated. The volcanic-like burst changes in Pd

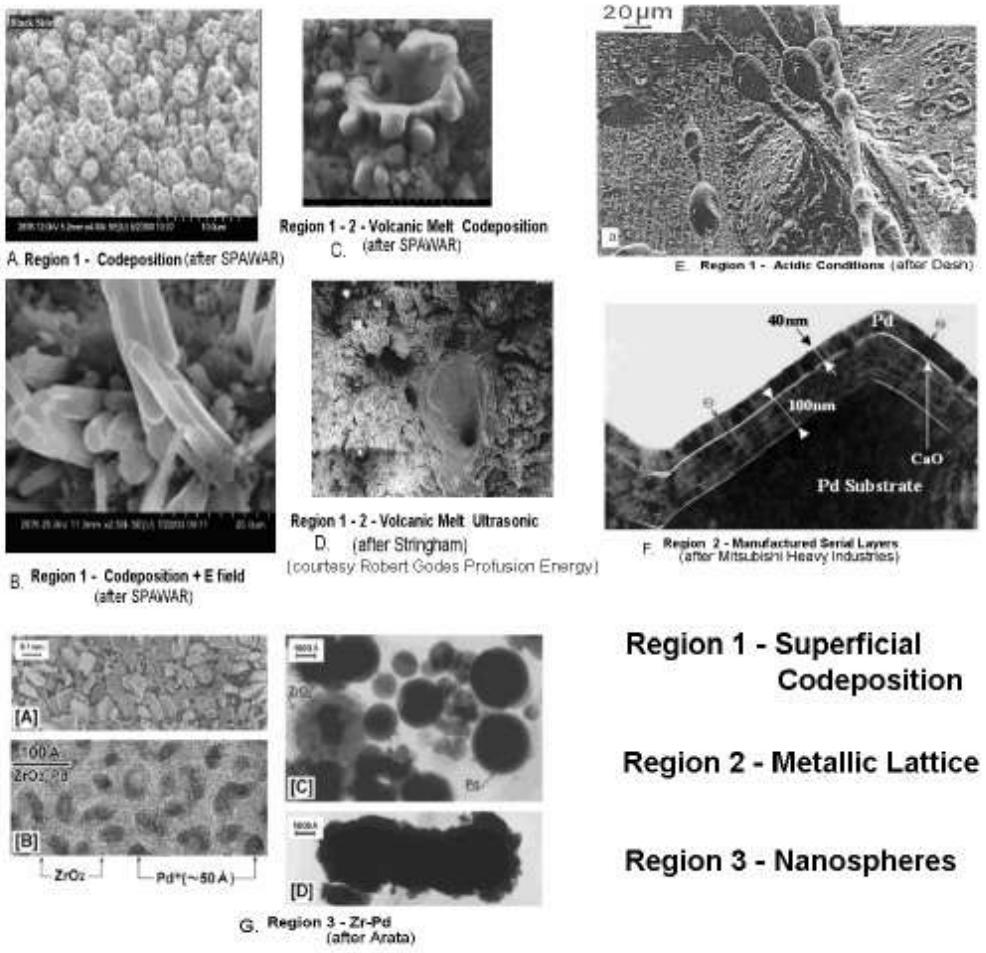

Figure 2. Three types ("regions") of palladium LANR

seen with SPAWAR codeposition and cavitation LANR in thin Pd foils loaded by "sonofusion" [23] suggest melting and subsequent re-solidification of molten metal, reminiscent of nuclear fission fuel metal damage (spontaneous Californium "spike damage"). The top middle image shows the occasional local melting of the palladium surface (C), presumably from the desired reactions. Below it, in the center is a Pd melt cavity produced by cavitational LANR reactions (D)[23]. To the top right, Fig. 1 shows morphologies (Image E) generated by acidic electrolysis generating nanotubes [8].

Located deeper in the metal, subsurface Region 2 in LANR yields heat and helium production and transmutation products. It includes the metallic lattice physically located beneath Region 1, existing as a thin rim under the surface in the range of 40 microns to millimeters. Subsurface sites (Region 2) yield heat and helium production and transmutation products. Below on the right side bottom of Fig. 1 are detailed Pd fabrication layers (Image F), 40–100 nm wide with a thin CaO layer intercalated [10].

Region 3 is a special state and size of nanostructures which are typically of width 7–30 nm and which efficiently

yield heat and helium production. These are found in deuterided palladium-black, palladium-black dual cathode [3], and glass ZrO palladium-black systems. Below on the left side bottom of Fig. 1 are Prof. Y. Arata's [3] nanomaterials (Image G) made from zirconium, leading to spherules [50,51].

3. Metamaterials in LANR

LANR devices can be greatly expanded by metamaterial shape which adds incredible properties beyond those of the material itself (definition of a 'metamaterial'). Metamaterials, through their unique, novel structures, can make previously "impossible" effects occur. Metamaterials [32,72–90] change the properties of materials by specific, precise, shapes; their stereoconstellation. Then, metamaterials have surprising, physical characteristics that defy earlier expectations, yet each produce solid, indelible experimental results. Metamaterials create negative refractive index materials [72,73], electromagnetic cloaking (and not just screening) [74], a simultaneous negative phase and group velocity of light [75], anomalous reflections and excitations of surface waves [76], isotropic lenses [77], and soliton decoherence [78]. Metamaterials come in arrays [81,82] and sol-gel composites [83] and are useful as novel antennae, filters, waveguides, and artificial magnetic media [82].

As Table 1 shows, consideration of metamaterial shape can improve excess heat power gain by 4–14 dB. This improvement in power gain results directly from the fact that the metamaterial shape changes where the steady state electric field distribution ends up; inside the LANR material resulting in a continual hydrogen flux.

Years of experimental suggests that metamaterials are critical for successful LANR. Over 20 years, well-controlled experiments using certain D-loaded devices have yielded impressive energy gain with fairly good reproducibility in time-integrated runs producing excess power gains in $Pd/D_2O/Pt$, $Pd/D_2O/Au$, and $Ni/H_2O_xD_2O_{1-x}/Pt$ LANR systems. Specifically, the uniquely shaped spiral Phusor®-type cathode, located opposite a platinum anode, has stood out for reproducibility, activity, power gain, and excess heat in this type of LANR system [32]. Its arrangement and stereoconstellation of electrodes appears to be one of the better arrangements for a LANR system, measured by activity and power gain [1–4,32]. Studies of more than a decade indicate a 4–14 dB gain from metamaterial technology. However, what was not clear until recently was why this occurs. It has been discovered that the spiral Phusor®-type cathode system with open helical cylindrical geometry in a high electrical resistance solution is a LANR metamaterial design which creates a unique and unusual electric field distribution, resulting in superior performance. To do this, Swartz and Verner used computed simulations based upon experimental findings to examine the impact of Phusor®-type LANR setups. Examined were geometric and other parameters of both the wire-wire and wire-Phusor system (Fig. 3) upon the electrical field distribution.

Dimensional (2D) vector electric field distributions are shown in Fig. 3 with the first case being that of two parallel, infinitely long, wire electrodes (anode at the top, and cathode below). The second case is a wire-Phusor system. In cross-section, the complex structure is approximated. The anode is at the top, and the cathode in each pair is located below it. Each cathode is electrically polarized against, and physically located opposite, an anodic wire of platinum. In a 2D view around a simple cathode wire, there is a near isotropic distribution of the E-field (Fig. 3). However, with the Phusor, there is a distinguishing electric field distribution different from customary wire-wire and plate-plate systems. The important secondary result is that when the Phusor®-type LANR metamaterial structure alters the electric field distribution, it produces continuous deuteron flux within the loaded palladium. The portion of the cathode vicinal to the anode has a higher than normal internal electric field intensity within its bulk volume. This does not characterize the two wire situation.

With the metamaterial LANR cathode configuration, there is an intrapalladial deuteron flow ("flux"), in addition to – and after – deuteron loading through portions of the cathode. The intraelectrode deuteron flux is through the metal, itself. This is reasonable because real palladium is not a perfect conductor, and in four terminal measurements of this sensors demonstrates resistances ranging from 40 to $\sim$ 120 mΩ. Most relevant to LANR, this intrapalladial deuteron

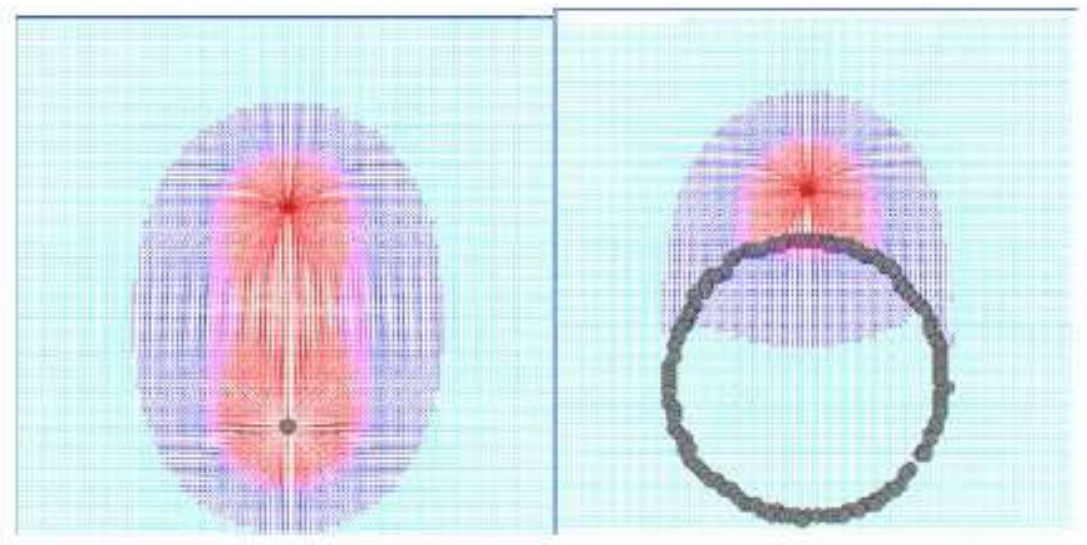

Figure 3. Phusor LANR Cathode in High Electrical Resistance Solution Left - 2-D vector electric-field distribution for two wire electrodes. Right - 2-D vector E-field distribution for PHUSOR®-type LANR system.

flow continues at equilibrium, similar to the microscopic semiconductor flux of holes and electrons at a p-n junction. We suspect that this additional type of deuteron flow is critical and enabling to LANR results. The results here support this, as do those of Violante [48] and Iwamura [10].

4. Deuteron Flux in LANR

Deuteron flux is key in LANR and there are two important points. First, metamaterials change the location of the flux, and second, mathematical solution requires the differential equations of continuum electromechanics. Nernst calculations of the activities of electrolyte [91,92] adjacent to a metal electrode have been applied to LANR to derive distributions of deuterium in the palladium and solution. However, because these LANR systems are not at equilibrium, the Nernst

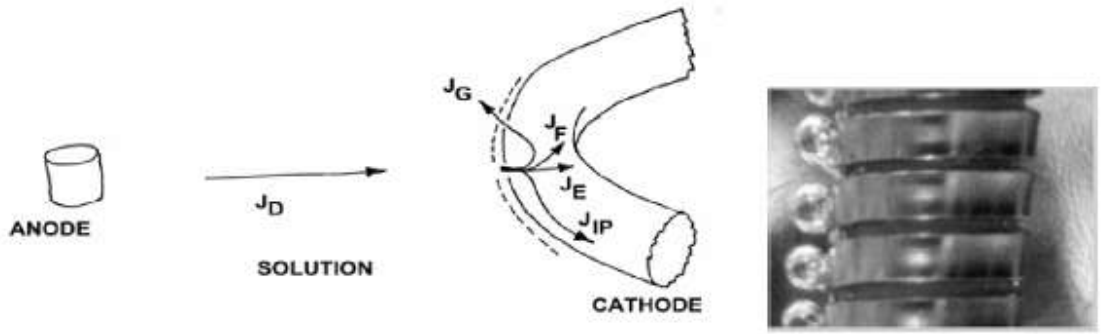

Figure 4. Metamaterial E-Field Distribution. (a) Left – Schematic of electrochemical loading, showing the fluxes of deuterons. (b) Right – Close-up of cathode showing asymmetric bubbling.

calculations are not applicable [52,53]. By contrast, and uneffected by non-equilibrium, the quasi-1- dimensional (Q1D) model of deuteron loading [52] analyzes the deuteron populations and the deuteron flow. It has foundation in the complex dielectric properties of materials [93] and continuum electromechanics [94]. Here, it has generated the deuteron-flux equation which explains some of the reasons for the difficulty in achieving LANR success. In the Q1D model, the different deuteron populations, their fluxes, and their locations (changed by the metamaterial shape) must be distinguished. They are seen in Fig. 4. On the left of Fig. 4 is a schematic representation of the anode, solution, and a portion of the cathode along with five types of deuteron fluxes involved in LANR. The deuteron fluxes are deuteron cationic flow in the solution (J_D), and the four types of deuteron flux in and near the loaded palladium cathodic metal lattice (J_E, J_G, J_F, and J_{IP}). The fluxes of deuterons in the metal include entry into the metal ("loading", J_E), gas (D_2) evolution ("bubble formation", J_G), intrapalladial deuteron flux (J_{IP}) flow through the metal, and an extremely tiny loss by fusion reactions (J_F). The continuous, equilibrium, flux of deuterons within the cathode (J_{IP}), produced by LANR metamaterials, is heralded by an observed unusual bubbling pattern, with spatial anisotropy, and synchronous with the excess heat. Referring to Fig. 4, this is shown on the right hand side.

Cationic deuteron flux (J_D) brings deuterons to the cathode surface. It begins far from the cathode surface, in the deuterium oxide (heavy water) located between the electrodes, where the deuterons are tightly bound to oxygen atoms as D_2O.

$$\boldsymbol{J}_D = -\boldsymbol{B}_D * \frac{d[D(z,t)]}{dz} - \mu_D * [\boldsymbol{D}(z,\boldsymbol{t})] * \frac{d\Phi}{dz}.. \tag{1}$$

In the absence of significant solution convection, the flux of deuterons (J_D) results from diffusion down concentration gradients and electrophoretic drift by the applied electric field [93–96]. J_D in the heavy water includes D-defects [95,96] driven by the applied electric field intensity to create a cathodic fall and double layer before the electrode surface. J_D depends on deuteron diffusivity (B_D) and electrophoretic mobility (μ_D), and the applied electric field intensity. Φ is the potential, the spatial gradient of which produces the electric field intensity. At any molecular site across the heavy water solution, the applied electrical energy is a tiny fraction compared to $k_B^* T$, so the deuterons migrate by drift ellipsoids of L− and D-deuteron defects in the applied electric field creating a ferroelectric inscription [95,96]. This D-defect conduction/polarization process augments other charge carriers, ionic drift, space charge polarization, and clathrates. The resultant D-defect migration produces a "cathodic fall" of deuterons and a E-field contraction so that most of the voltage drop is at the interface in front of the electrode surface. This concentration polarization may produce very large local electric field intensities, possibly ranging from 10^4 to 10^7 V/cm, resulting in a very large electrical potential drop across a small distance vicinal to the cathode.

Just beyond that, at the inner boundary of the double layer, intermolecular deuteron transfer from the heavy water solution to the metal surface, controlled by electron- limited transfer, leaves an atomic deuteron on the metal surface. This leaves an atomic deuteron attached to the metal surface, with its next transfer controlled by the metallurgy of the thin interfacial region possibly a few Angstroms thick, by the applied electric field intensity, and by the local concentrations of deuterons and quenching materials. The entry mechanisms to the palladium surface are driven by infrared vibrations and microwave rotations [95], creating a solution photosensitivity which produces a photoactivated increase of excess energy and loss of power gain [33].

At the surface of the low hydrogen-overvoltage palladium, there exist surface atomic (D) and diatomic (D_2) deuterons and some which also enter ('load') the bulk metal [52,53,1–3,32] or transit through the metal by intrapalladial deuteron flow if a metamaterial is used under select conditions. The gas bubbles (D_2) are undesirable producing low dielectric constant layers in front of the electrode, obstructing the electrical circuit. Any deuterons which enter the metal are electrically neutralized ('dressed') by a partial electronic cloud, shielding their charge (in a Born–Oppenheimer approximation) [38]. The deuterons drift along dislocations, and through the lattice and its vacancies as interstitials, falling from shallow to more deeply lying (energetically) binding sites. The deuteron drift is obstructed by ordinary hydrogen

and other materials blocking key interfacial sites and grain boundary dislocations.

It is the deuteron flow equations which explain the loading, the codeposition, the quenching effects, the metamaterial effects, and the optimal operating point manifolds. Numerically dividing each deuteron flux (J_E, J_G, and J_F) by the local deuteron concentration yields the first-order deuteron flow rates, k_E, k_G, and k_F (with units of cm/s, respectively). At the surface of the loading metal, using conservation of mass, Eq. (1) becomes Eq. (2), the deuteron flux equation of LANR.

$$\boldsymbol{\kappa}_e = (\boldsymbol{\mu}_D \mathbf{E}) - (\boldsymbol{\kappa}_g + \boldsymbol{\kappa}_f). \tag{2}$$

Equation (3) can be modified to Eq. (3) by substituting the Einstein relation.

$$k_e = \frac{B_D q V}{L[k_B T]} - (\kappa_g + \kappa_f). \tag{3}$$

Equation (3) is the modified deuteron loading rate equation, derived from geometric and material factors. B_D is the diffusivity of the deuteron. $k_B T$ is Boltzmann's constant and temperature. q is the electronic charge, and V is the driving applied voltage. There are many important lessons for LANR. First, dominating everything is the first term which now has the ratio of two energies (the applied electric energy organizing the deuterons divided by $k_B T$, thermal disorder). This energy ratio is decisive in controlling the deuteron loading flux in palladium. Successful LANR reflects the 'war' of organization by the applied electric field intensity which is organizing the deuterons versus their randomization by thermal disorder.

Second, the second term heralds that competitive gas evolving reactions at the metal electrode surface can destroy (quench) the desired reactions. Note that the first order loading flux rate constant (k_E) is dependent upon the applied electric field intensity minus the first order gas loss rate constant resulting from gas (D_2) evolution at the cathode (k_G). This implication is exactly opposite conventional "wisdom" that LANR is 'fusion by electrolysis' [1–4].

Third, detailed further analysis of Eq. (3) also suggests that LANR can be missed by insufficient loading, contamination (effecting k_E, by protons or salt), and by the evolution of D_2 gas, which all inhibit ("quench") the desired LANR reactions [3,4].

5. Optimal Operating Points In LANR

Success of LANR requires multiple factors including loading, adequate confinement time (sometimes weeks), loading rate, prehistory with careful preparation including absence of contamination and avoidance of materials which quench performance. We have reported that anomalous energy gain in metal deuterides became a more reproducible phenomenon as optimal operating point (OOP) understanding and technology [52–55] has been applied to LANR (JET Energy, 1–4; JWK, 57; Innoventek) [56]. Optimal operating points, and OOP manifolds, appear when the calibrated output data of an LANR device (producing amplified heat, excess power gain, de novo incremental helium-4 or tritium production) is presented as a function of the input electrical power (Fig. 5).

Figure 5 shows three LANR Optimal operating point (OOP) manifolds presenting power gain and *de novo* helium-4 and tritium production for conventional, high- impedance, codeposition and palladium-black nanomaterial LANR systems. The horizontal axis is the electrical power input (log watts). The vertical axis is uncalibrated and linear. The optimal operating point (OOP) is the relatively narrow peak of the biphasic LANR production curve when viewed as a function along the electrical input power axis. From an operational point of view, during situations in which excess power is generated from an active LANR sample or device, large changes in LANR output, such as excess power gain, are observed as the input power is varied over a relatively small range.

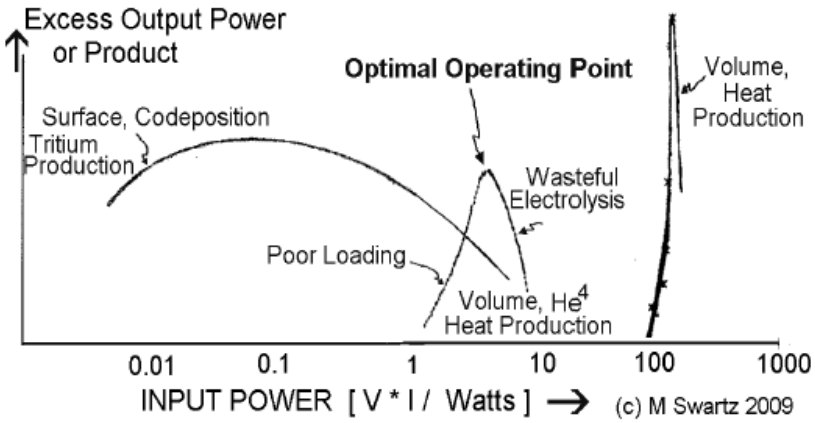

Figure 5. Three LANR optimal operating point (OOP) manifolds.

In Fig. 5, the central OOP manifold (curve) is for a Pd Phusor®-type LANR device, and has general overlap with the He^4 production curve [1,2,1,55–57]. The excess heat amounts to hundreds of thousands of joules of 'excess heat' per day [1,2]. The helium nuclei are generated in their first excited state, He^{4*}, which provides the lattice heating as the helium nucleus returns to its ground state in reactions which are consistent with nuclear [97–102], solid state [102–110], Mossbauer [111–113], and radiation physics [34,114]. The other two curves in Fig. 5 show how this LANR Optimal Operating Manifold compares to two other independent investigator setups involving nanomaterials (after Arata and Zhang) and tritium (after Szpak, Gordon, and Mosier-Boss). Charged particles, tritium [22,41,46,49], and low levels of particles and radiation [19,20,40] have been detected in some systems. Srinivasan from BARC (India) reported tritium and neutrons in 1989. John Bockris (Texas A&M) reported tritium in bursts, not accompanied by measurable heat. Szpak (SPAWAR) reported tritium in some codeposition systems. Miles and Srinivasan independently used dental X-ray films outside of their LANR to demonstrate fogging consistent with low energy x-ray production. Li (Tsinghua U), Larry Forsley (JWK International) and Mosier- Boss (SPAWAR) have used CR-39 to detect energetic charged particles, including D–D and D–T reactions [19,20].

OOPs and their manifolds are important for several reasons. First, organized this way (by input electrical power), the data formidably dispels the LANR "irreproducibility" myth. OOP manifolds make salient why LANR was so difficult to achieve in the first place. The optimal operating point is but one focus at which the system can be driven. The rest of the foci, other possible points at which the system can be driven, are the "optimal operating point manifolds".

OOP manifolds provide important information, and understanding, about LANR system response as input power is changed. In heat-producing LANR experiments, at lower values of the input power, he said the reaction rates of the desired reactions vanish or are low (usually because the loading is inadequate). At higher values of input power (associated with the region located to the right of any of the OOP manifold peaks), the output power is reduced for several reasons. These include losses in output energy from a reduced number of reactions, a secondary effect associated with gas bubble formation, and the combined effect of both sources of energy loss on the system. Driving with electrical input power beyond the peak optimal operating point (OOP) does not improve the production of the desired product, but instead yields a falloff of the production rates despite increasing input power. Many negative LANR reports occur due to a failure to operate the LANR system at, or near, the optimal operating point.

Second, LANR is better controlled. OOP operation allows control, better understanding, more reproducible operation, and much improved success of LANR systems with what preliminary studies indicate a 8–25 dB or more gain [1–4].

Third, OOP understanding enables one to standardize examination of specimens and materials, normalizing treatment of samples. OOP characterization allows determination of maximal sample activity (MSA).

Fourth, control of OOP manifolds have shown their worth by being proven useful to maximize and control secondary LANR effects including "heat after death" [30,31], the response to incident coherent optical radiation [33], and non-thermal near IR emission [34].

Fifth, OOPs and OOP manifolds are universal in LANR systems. OOPs characterize Pd-heavy water LANR induced incremental helium and tritium production, and the generated excess heat production, including for conventional and high impedance $Pd/D_2O/Pt$ and $Pd/D_2O/Au$ LANR systems and Phusor®-type LANR devices, and for $Ni/H_2O_xD_2O_{1-x}/Pt$ and $Ni/H_2O_xD_2O_{1-x}/Au$ LANR devices, and for codeposition systems and codeposition LANR devices, and for tritium generated from codeposition and conventional heavy water systems for excess heat and helium production in palladium-black systems for excess heat in light water nickel systems [1,55–57].

Sixth, slightly different OOP manifolds characterize each type of nanostructures ([50,51], called "3RH"). This group segregation is consistent with the complex behavior of palladium (Section 2), and a growing set of LANR experimental data [1–51], including 'heat-after-death (HAD) excess heat' evanescent decay kinetics [30,31].

6. Building LANR Nanostructures

Nanostructure preparation, assembly, and driving are very complicated and described elsewhere [1–4,35,38]. However, when the correct nanostructure is combined with the correct deuteron flux, and the system driven at the OOP, there is a higher likelihood of LANR success. Beneath the complicated generated nanostructures are very pure materials. In these group of experiments, the cathodes were prepared from 99.98 + % Pd (Alfa Aesar, Ward Hill, MA), 1.0 mm diameter, ∼4–7 turns on a spiral of ∼1.3 cm diameter, with a gap separation from the anode arranged in a $Pd/D_2O/Pt$ or $Pd/D_2O/Au$ configuration (Pt 99.998%). The cathodes have four leads, supporting in situ four terminal electrical conductivity measurement. The solution is very low electrical conductivity heavy water (deuterium oxide, low paramagnetic, 99.99%, Cambridge Isotope Laboratories, Andover MA) with no additional electrolyte. The low electrical conductivity water bathed the spiral cathode. Contamination remains a major problem, with excess heat devastatingly quenched by increasing electrical conductance of the solution [2–4] and effects on the cathode. Contaminants appear from both electrode and container degradation and leeching, from atmospheric contamination, and after temperature cycling. These all inexorably, unintentionally, add to the electrolytic solution decreasing the level of deuteron loading achieved, the rate of loading as well, and the maximum heat producing activity. The heavy water is hygroscopic, therefore kept physically isolated from the air by seals, including several layers of Parafilm M (American National Can, Menasha, WI) and paraffin. We continue to avoid chlorine or chloride because of possible explosions. This is due to visible light ignition susceptibility, which results because the activation energy with chlorine is only ∼17 μJ.

The loading of the palladium from the heavy water, and driving of the reactions through the two electrodes within the reaction container was obtained by controlled electric current source, or a Keithley 225 at low input, with ±1% accuracy. Electrical voltage sources included HP/Harrison 6525A for transsample potentials up to 3000 V (∼ ±0.5% accuracy). All connections isolated, when possible, with Keithley electrometers for computer isolation. For 4-terminal intra-electrode Palladium electrical conductivity measurements, a first Keithley 225 electric current source was used to drive the cell, and load the Phusor. A second Keithley 225 electric current source was used to drive the electrical current portion of the four terminal electrical conductivity measurement of the palladium. All leads near the solution were covered with electrically-insulating tubes (medical grade silicone, Teflon, or proprietary materials) used to electrically isolate wires.

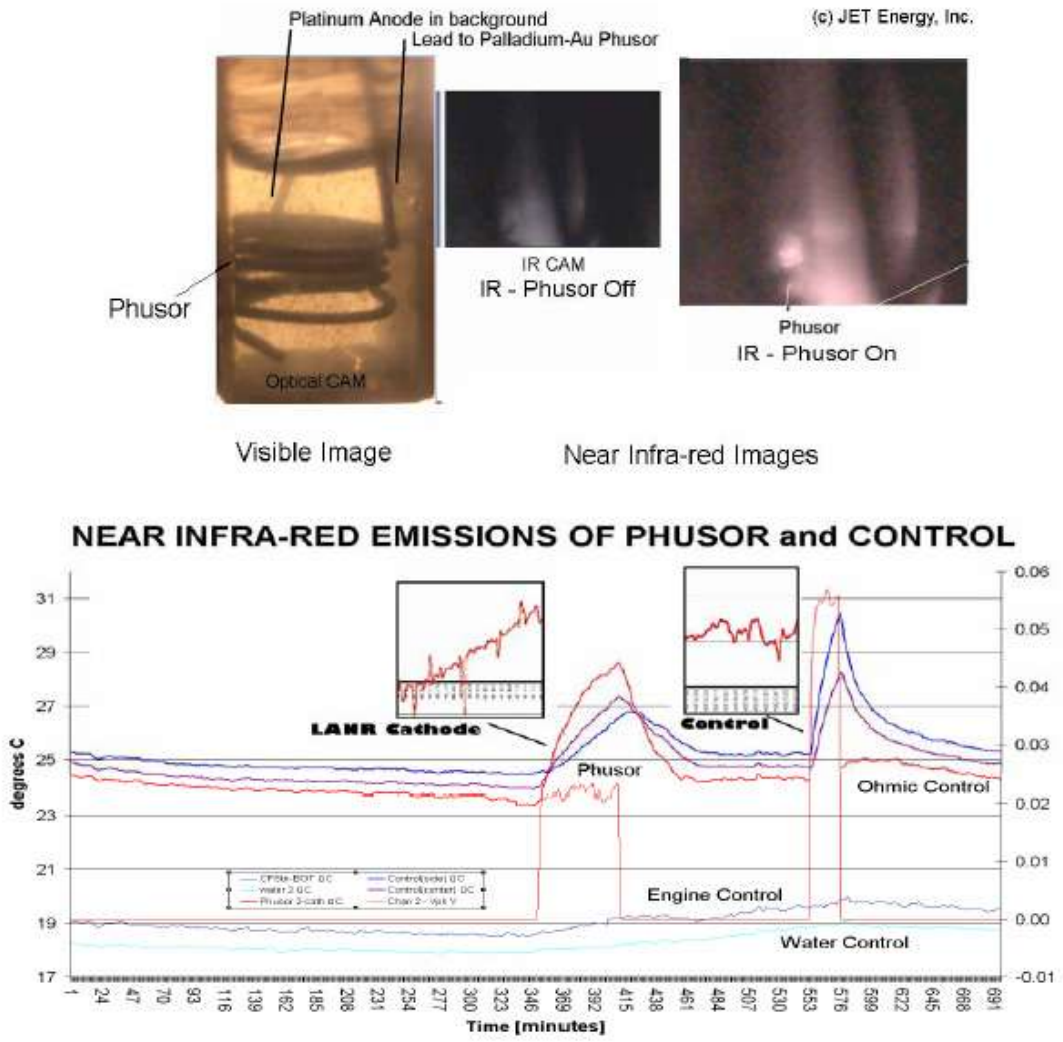

Figure 6. (above) Visible and IR Images of DAP LANR Cell, Before and After Activation

The data from voltage, current, temperatures at multiple sites of the solution, and outside of the cell, the 4-terminal measurement of the cathode's internal electrical conductivity, additional calibration thermometry and other measurements were sampled at 0.20 Hz, usually 1 Hz, 22+ bits resolution (Omega OMB-DaqTemp (Omega; voltage accuracy $0.015^{\pm 0.005}$ V, temperature accuracy <0.6°C) and recorded by computed DAQ. To minimize quantization noise, 1 min moving averages were sometimes made. The noise power of the calorimeter is in the range of ∼1–30 mW. The noise power of the Keithley current sources is ∼ 10 nW. Input power is defined as V*I. There is no thermo-neutral correction in denominator. Therefore, the observed power is a lower limit. The instantaneous power gain (power amplification factor(non-dimensional)) is defined as Pout/Pin, as calibrated by at least one electrical joule control [ohmic

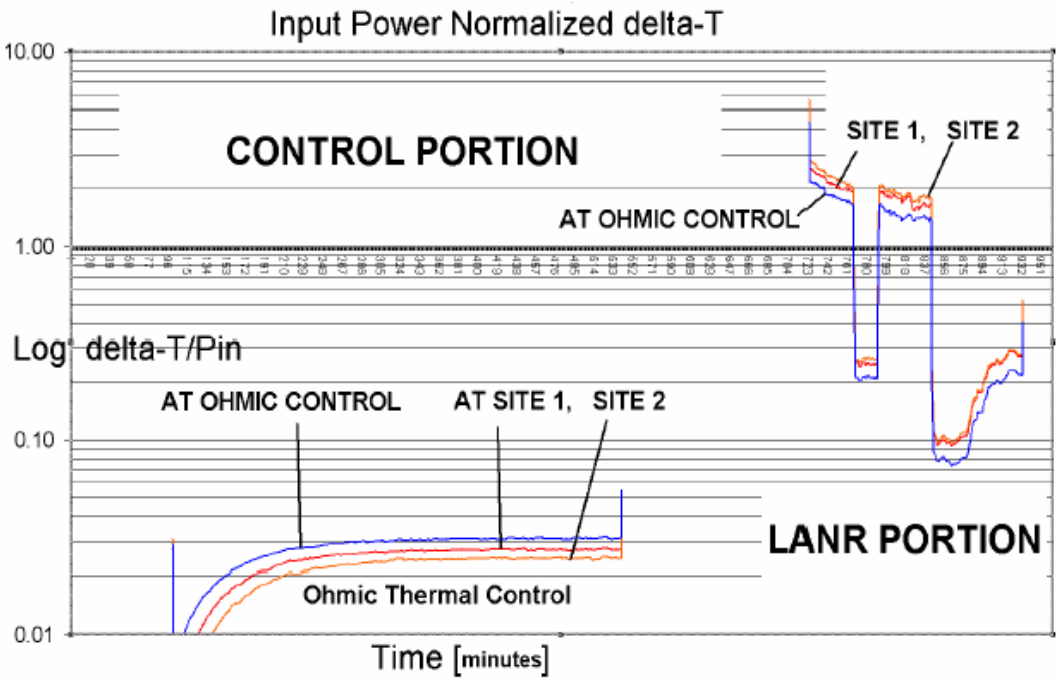

Figure 7. Input power normalized delta-T curves for DAP Phusor® LANR

resistor] and time integrated for validation. The excess energy, when present, is defined as (Poutput - Pinput) * time. The amount of output energy is interfered from the heat released producing a temperature rise, which is then compared to the input energy.

The codepositional high impedance devices and the DAP (Dual anode Phusor®- Type LANR device; Pd/D_2O, $Pd(OD)_2/Pt-Au$) were generated as discussed elsewhere [2–4,34]. For the DAP Phusors, palladium is laid down from a sacrificial anode upon the surface of a virgin palladium cathode. Then, the palladium anode is removed, and replaced by a gold wire anode to stop the further laying down of further palladium nanostructure upon the palladium cathode. Interestingly, we have reported a new phenomenon during codepositional layering of the DAP Phusor cathode. This consists of a dynamic instability, observed as an oscillation, heralding an electrohydrodynamic Rayleigh–Taylor or Bernard instability which is associated with the layering. The time constant was circa 15 min per cycle, but this was irregularly irregular, with three to five cycles occurring in a 60 min period.

For Figs. 6 and 7, Pd and D were electrodeposited and the excess heat was measured when the thickness was circa 17,000 atoms deep over the deposited area, with a total area of 2.57 cm^2. At that time, the solution was 7.7 mmol $Pd(OD)_2$, and the open circuit voltage, V_{oc}, used to determine the effectivity of LANR [2,3], was 1.46 V. The $Pd^*/D_2O-Pd(OD)_2/Au$ Phusor®-type system has an initial cell resistance of circa 868 kilohms. During development of the nanostructure this falls to circa 48.3 kΩ and less.

Temperature measurements are made by specialized electrically -insulated thermocouples (accuracy ±0.8 K, precision ±0.1 K), RTD and other sensors. Probes were calibrated by Omega IcePoint Cell and core temperatures were maintained by feedback control using a Yellow Spring Thermal Controller Model 72 (bandwidth of 0.2 K) within a Honeywell water circulation zone controlled room (±2.5 K). Thermocouples and other temperature sensors decorated

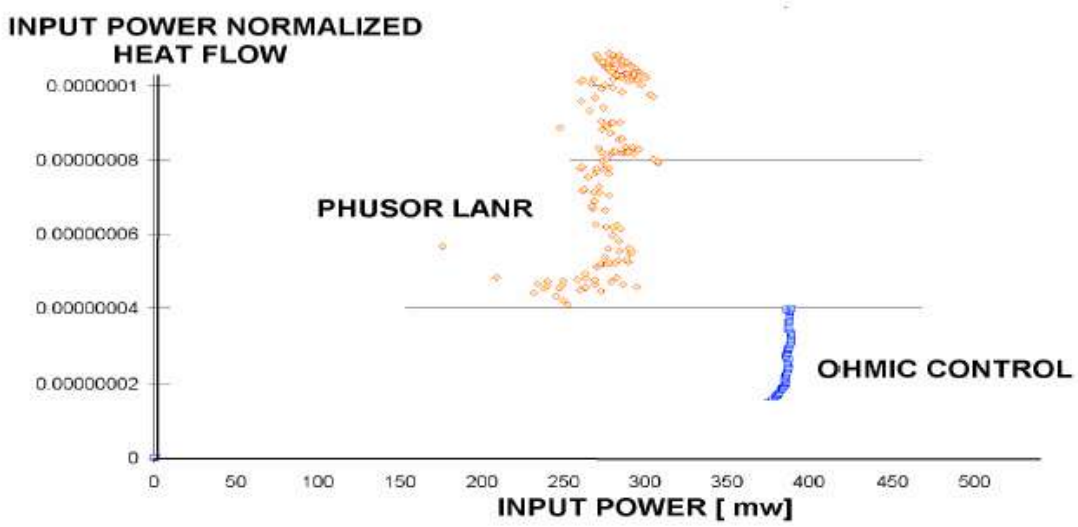

Figure 8. DAP LANR Device Heat Flow Output

the periphery of the cell, and a multicompartment calorimeter was used. There was an additional heat-flow probes at the periphery outside of the core. To minimize contamination, the majority of temperature measurements were outside of the inner core container. Calorimetry is augmented by heat flow measurement, electricity production using thermo-electrics, and LANR-driven motors. Outputs are calibrated by ohmic (thermal) controls, and dual ohmic (calorimeter) controls, to evaluate, and certify possible excess heat. Additional calibration has included adequate Nyquist sampling, time- integration, thermal ohmic controls, waveform reconstruction, noise measurement, and other techniques [2–4].

The near IR Imaging is complicated. Dr. Stan Szpak (SPAWAR) et alia reported the emission of infra-red from LANR codeposition devices. However, they did not use a control, and there have been questions concerning both the linearity and calibration of their single effort. SPAWAR and JET Energy have investigated the physical changes, the excess heat generation, hot spots with additional controls by JET Energy demonstrating non-thermal near IR emission (Fig. 5). We have examined the impact of laser irradiation on LANR cathodes, and reported in 2003 that part of the impact is due to reflection off of the cathode back into the double layer. There, deuteron injection into the palladium increases (activation energy of $\sim$14 kcal/mol) from microwave rotation and IR vibration for the intermolecular transfer of deuterons to the Pd [33]. Hagelstein, Letts and Cravens [11,12] have reported both single and dual photon impacts on cathodes.

In our near IR (NIR) LANR studies, we initially, incorrectly, thought a single control (vs. Szpak et al. who had used no controls) would be needed. It was soon discovered that two controls are needed. Thereafter, calibration included normalization of NIR emission intensities to both non-energized environmental and to ohmic control areas, supplementing semiquantitative calibration against an ohmic thermal control. NIR data capture was by slow scan near-IR and visible videocam ($\sim$ 1 Hz). Thereafter information was obtained by analysis using semiquantitative computed measurements of collected NIR output, integrated over both the DAP cathode, the ohmic thermal control, and their environment as they were each activated or not. The integrated NIR output of serial computed images of the DAP Phusor® and ohmic control were compared by normalization to the controls, and examined as a function of time.

Matched arrays of solar cells integrated the recorded near-IR emissions of the DAP device, the thermal control, and the control areas over time.

7. NT-NIR and XSH from LANR Nanostructures

Correctly driven, LANR nanostructures fabricated as LANR metamaterials exhibit significant excess heat, excess heat flow, and non-thermal near infrared (NT-NIR) emission linked to both. Figure 6 shows three visible and near-infrared (NIR) views of a DAP codeposition Phusor®-type LANR device in heavy water. The platinum anode is seen in the background. The DAP Phusor® is located in both images ($\sim$ 7.7 mmol Pd(OD)2). The first view is in ordinary light, the other two (from a slightly different angle of observation) are in the near infrared (NIR). The two images on the left preceed (controls, "off"), and the one on the right is after, activation and generation of excess heat. As in other experiments involving a variety of LANR metamaterial spiral-wound and other Phusor®-type lattice assisted nuclear reaction (LANR) systems, including high impedance palladium ($Pd/D_2O/Pt$, $Pd/D_2O/Au$), codepositional ($Pd/Pd(OD)_2/Pt$) heavy water, and nickel ($Ni/H_2O_xD_2O_{1-x}/Pt$, $Ni/H_2O_xD_2O_{1-x}/Au$) light water Phusor-type LANR devices [34], there is a linkage of excess power gain and heat flow with simultaneous NT-NIR emission. (below) Non-Thermal Near IR Emission at the Optimal Operating Point during Excess Heat Generation

There are several important findings and secondary implications. First, the emission of near-IR from the electrodes when excess heat is only observed when active electrodes operated at their optimal operating point, and then NT-NIR is linked and specific to the LANR devices' excess heat production and not its physical temperature. The estimate of the color temperature during NT-NIR of for these LANR devices, driven at their optimal operating point and input power drive levels, was estimated at $\sim$500–1000 K.

Second, these findings confirm the Bremsstrahlung-shift hypothesis [114] which states that in LANR, distinct from hot fusion, there is a temperature-related shift from hot fusion's penetrating ionizing radiation to LANR's skin-depth-locked infrared radiation. Simply put, unlike hot fusion or plasma systems, bremsstrahlung radiation in LANR systems cannot dissipate fusion derived excess power through penetrating radiation. The Bremsstrahlung radiant power density falls from 0.05–0.28 (hot fusion) to 1.4–8.1 $\times 10^{-10}$ for LANR. The delivered X-ray dose at 1 m decreases by 11–18 to 23 orders of magnitude, saving the graduate students, from 3.1×10^{19} Grays (hot fusion) to 1.4–3.3×10^{-4} Grays for LANR. This is consistent with the relative absence of ionizing emissions from most cold fusion systems, except for a few reports looking in the $\sim$6–20 keV region. In addition, the temperature difference also causes the output spectrum of the Bremsstrahlung radiation to be shifted to the near infra-red, consistent with the NIR emission of LANR systems at their OOP.

Third, with control of LANR by precise material fabrication, metamaterial shape selection using high impedance ("High-*Z*") Phusor®-type LANR devices in very low electrical conductivity D_2O, control of D-flux and post D-loading flux, there is a higher likelihood of achieving LANRs impressive energy gain with fairly good reproducibility. Such high impedance LANR devices have shown power gains 200–400%, and higher, compared to input energy and to input energy transferred to conventional dissipative devices.

Figure 7 shows the ephemeral superlative output of one DAP Phusor(R) type LANR device. The graph shows the input power-normalized change in temperature (degrees centigrade, delta-T) for both the ohmic thermal control and the DAP Phusor. When activated, the DAP ($Pd^*/D_2O - Pd(OD)_2/Au$ Dual Anode Phusor®-type), the peak power gain was circa 8000% (Fig. 6) which led to damage of the leads of the cell (Fig. 7).

Figure 8 shows the output for a heat flow sensor arranged to receive some of the heat output from both the DAP Phusor and the ohmic control. The data is the electrical output of the heat flow sensor normalized by the input electrical power. It can be seen that the DAP Phusor produced more heat flow normalized for power for input power, then did the ohmic thermal control. Excess power gain was $\sim$500% based on the heat flow sensors.

In the future, LANR will become an energy multiplier because the energy density of LANR reactions is ten million

times that of gasoline. Given the prevalence of the fuel, and the incredible efficiency, LANR will play a critical role in all future technologies with potential revolutionary applications to all energy issues – robotics, transportation, electricity production, and space travel.

Acknowledgments

The author thanks Gayle Verner for her meticulous help in manuscript and idea development, and also Jeffrey Tolleson, Alex Frank, Alan Weinberg, Allen Swartz, Charles Entenmann, Frank Gordon, Larry Forsley, Pamela Mosier-Boss, Brian Ahern, Jeff Driscoll, Peter Hagelstein, Robert Smith, Jan Marwan, and the late Scott Chubb for their helpful conversations, and JET Energy and New Energy Foundation for the support. PHUSOR® is a registered trademark of JET Energy, Incorporated. PHUSOR®-technology is protected by U.S. Patents D596724, D413659 and Patents pending.

References

[1] M.R. Swartz, Survey of the observed excess energy and emissions in latticeassisted nuclear reactions, *J. Scientific Exploration* **23**(4) (2009) 419–436.

[2] M.R. Swartz, Excess power gain and tardive thermal power generation using high impedance and codepositional phusor type LANR devices, in *ICCF-14 Int. Conf. on Condensed Matter Nuclear Science*, Washington, DC, 10–15 August 2008, David J. Nagel and Michael E. Melich (Eds.), ISBN: 978-0-578-06694-3, 123, 2010.

[3] M. Swartz, G. Verner, Excess heat from low electrical conductivity heavywater spiral-wound Pd/D_2O/Pt and Pd/D_2OPdCl_2/Pt devices, Condensed Matter Nuclear Science, Proc. of ICCF-10, P.L. Hagelstein, S. Chubb (Eds.), World Scientific, NJ, ISBN 981-256-564-6, 29-44; 45-54 (2006).

[4] M. Swartz, Consistency of the biphasic nature of excess enthalpy in solid state anomalous phenomena with the quasi-1-dimensional model of isotope loading into a material, *Fusion Technol*. **31** (1997) 63–74.

[5] Y. Arata and Y.C. Zhang, Anomalous Production of Gaseous ^{4}He at the Inside of DS-cathodedDuring D_2-electrolysis, Proc. Jpn. Acad. Ser. B, 75, p. 281 (1999); Y. Arata and Y.C. Zhang, Observation of anomalous heat release and helium-4 production from highly deuterated fine particles, *Jpn. J. Appl. Phys.* Part 2, **38** (1999) L774; Y. Arata and Y. Zhang, The establishment of solid nuclear fusion reactor, *J. High Temp.* Soc. **34**(2) (2008) 85.

[6] F. Celani et al., Deuteron electromigration in thin pdwires coated with nano-particles: evidence for ultra-fast deuterium loading and anomalous, large thermal effects, in *ICCF-14 Int. Conf. on Condensed MatterNuclear Science*, Washington, DC, 2008.

[7] I. Dardik and H. Branover, A. El-Boher, D. Gazit, E. Golbreich, E. Greenspan, A. Kapusta, B. Khachatorov, V. Krakov, S. Lesin, B. Michailovitch, G. Shani and T. Zilov, Intensification of low energy nuclear reactions using superwave excitation, *Proc. 10th Int. Conf. on Cold Fusion* (2003).

[8] J. Dash and D.S. Silver, Surface studies after loading metals with hydrogen and/or deuterium, 13th Conf. CMNS 2007, Sochi, Russia; J. Dash and S. Miguet, Microanalysis of Pd cathodes after electrolysis in aqueous acids, *J. New Energy* **1**(1) (1996) 23.

[9] M. Fleischmann and S. Pons, Electrochemically induced nuclear fusion of deuterium, *J. Electroanal. Chem.* **261**, 301–308, erratum **263** (1989) 187; M. Fleischmann and S. Pons, Some comments on the paper Analysis of experiments on calorimetry Of LiOD/D_2O electrochemical cells, R.H. Wilson et al., *J. Electroanal. Chem.* **332** (1992) 1?, *J. Electroanal. Chem.* **332** (1992) 33–53, M. Fleischmann, and S. Pons, Calorimetry of the Pd–D_2O system: from simplicity via complications to simplicity, *Phy. Lett.* A **176** (1993) 118–129, M. Fleischmann, S. Pons, M. Anderson, L.J. Li and M. Hawkins, Calorimetry of the palladium–deuterium-heavy water system, *Electroanal. Chem*. **287** (1990) 293.

[10] Y. Iwamura, M. Sakano and T. Itoh, Elemental analysis of Pd complexes: effects of D_2 gas permeation. *Jpn. J. Appl. Phys.* A **41** (2002) 4642, Y. Iwamura et al., Observation of surface distribution of products by X-ray fluorescence spectrometry during D_2 gas permeation through Pd complexes, in *12th Int. Conf. on Condensed Matter Nuclear Science*, 2005, Yokohama, Japan.

[11] D. Letts and D. Cravens, Laser stimulation of deuterated palladium: past and present, *Proc. 10th Int. Conf. on Cold Fusion*, Cambridge, MA, 2003.

[12] D. Letts and P.L. Hagelstein. Stimulation of optical phonons in deuterated palladium, in *ICCF-14 Int. Conf. on Condensed Matter Nuclear Science*, 2008, Washington, DC, D. Letts, D. Cravens and P.L. Hagelstein, *Thermal Changes in Palladium Deuteride Induced by Laser Beat Frequencies*, in Low-Energy Nuclear Reactions Sourcebook, J. Marwan and S. Krivit (Eds.), 2008

[13] M. McKubre, F. Tanzella, P.L. Hagelstein, K. Mullican and M. Trevithick, The need for triggering in cold fusion reactions, Proc. *10th Int. Conf. on Cold Fusion*, Cambridge, MA, 2003.

[14] M.H. Miles, R.A. Hollins, B.F.Bush, J.J. Lagowski and R.E.Miles, Correlation of excess power and helium production during D_2O and H_2O electrolysis, *J. Electroanal. Chem.* **346** (1993) 99–117.

[15] M.H. Miles and B.F. Bush, Heat and helium measurements in deuterated palladium, *Trans. Fusion Technol.* **26** (1994) 156–159.

[16] M.H. Miles et al., Calorimetric analysis of a heavy water electrolysis experiment using a Pd–B alloy cathode, Naval Research Laboratory Report NRL/MR/6320-01-8526, 155 pp., March 16, 2001.

[17] G.H. Miley, G. Narne and T.Woo, Use of combined NAA and SIMS analyses for impurity level isotope detection, *J. Radioanal. Nucl. Chem.* **263**(3) (2005) 691–696, G.H. Miley and J. Shrestha, Transmutation Reactions and Associated LENR Effects in Solids, in *Low-Energy Nuclear Reactions Sourcebook*, J. Marwan and S. Krivit (Eds.), Oxford University Press, Oxford, 2008.

[18] P.A. Mosier-Boss and S. Szpak, The Pd/nH system: Transport processes and development of thermal instabilities, *Il Nuovo Cimento* **112**A (1999) 577–585.

[19] P.A. Mosier-Boss, S. Szpak, F.E. Gordon and L.P.G. Forsley, Use of CR-39 in Pd/D co- deposition experiments, *Euro. Phy. J. Appl. Phy.* **40** (2007) 293–303.

[20] P.A. Mosier-Boss, S. Szpak, F.E. Gordon and L.P.G. Forsley, Triple tracks in CR-39 as the result of Pd–D co-deposition, evidence of energetic neutrons, *Naturwissenschaften* **96** (2008) 135–142.

[21] S. Pons, and M. Fleischmann, Heat after death, *Proc. ICCF-4*, Maui, EPRI TR104188-V2, 2, 1994, pp. 8-1, **Trans. Fusion Techol. 26**(4T), Part 2 (1994) 87.

[22] M. Srinivasan et al., Tritium and excess heat generation during electrolysis of aqueous solutions of alkali salts with nickel cathode, *Frontiers of Cold Fusion*, H. Ikegami (Ed.), *Proc. Third Int. Conf. on Cold Fusion*, October 21–25, 1992, Universal Academy Press, Tokyo, pp. 123–138.

[23] R. Stringham, Cavitation and fusion, *ICCF-10*, 2003, Cambridge, MA.

[24] M. Swartz, Can a Pd/D_2O/Pt device be made portable to demonstrate the optimal operating point? Condensed Matter Nuclear Science, *Proc. Of ICCF-10*, Peter L. Hagelstein and Scott R. Chubb (Eds.), World Scientific, NJ, ISBN 981–256–564–6, 29–44; 45–54, 2006.

[25] M. Swartz, Codeposition of palladium and deuterium, Fusion Techol. 32 (1997) 126–30.

[26] M. Swartz, Noise Measurement in cold fusion systems, *J. New Energy* **2**(2) (1997) 56–61.

[27] M. Swartz, Patterns of failure in cold fusion experiments, Proc. *33rd Intersociety Engineering Conf. on Energy Conversion*, IECEC-98-I229, CO, Aug. 1998.

[28] M. Swartz, Patterns of success in research involving low-energy nuclear reactions, *Infinite Energy* **31** (2000) 46–48.

[29] M. Swartz, The Impact of heavy water (D_2O) on nickel-light water LANR systems, Proc. *9th Int. Conf. on Cold Fusion*, Beijing, China, Z. Xing and X. Li (Eds.), May 2002.

[30] M. Swartz and G. Verner, Dual ohmic controls improve understanding of 'heat after death, *Trans. Amer. Nucl. Soc.* **93** (2005) 891–892. ISSN:0003-018X.

[31] M. Swartz, and G. Verner, Two sites of cold fusion reactions viewed by their evanescent tardive thermal power, Abstract, ICCF-11 (2004), M. Swartz (Ed.), *Kinetics and Lumped Parameter Model of Excess Tardive Thermal Power*, Mitchell Swartz, APS, 2005.

[32] M. Swartz, G. Verner, Metamaterial Function of Cathodes Producing Hydrogen Energy and Deuteron Flux, *Proc. 14th Int. Conf. Condensed Matter Nucl. Sci. and the 14th Int. Conf. Cold Fusion (ICCF-14)*, 10–15 August 2008, Washington, DC, David J. Nagel and Michael E. Melich (Eds.), ISBN: 978-0-578-06694-3, 458, 2010.

[33] M. Swartz and G.Verner, Photoinduced excessheat from laser-irradiated electrically-polarized palladium cathodes in D_2O, Condensed Matter Nuclear Science, *Proc. ICCF-10*, Peter L.Hagelstein and Scott Chubb (Eds.), NJ, ISBN981-256-564-6, 213-226, 2006.

[34] M. Swartz and G.Verner, A.Weinberg, Non-thermal near-IR emission linked with excess power gain in high impedance and

codeposition phusor-LANR Devices, in *Proc. 14th Int. Conf. Condensed Matter Nucl. Sci. and the 14th Int. Conf. Cold Fusion (ICCF-14)*, 10–15 August 2008, Washington, DC, David J. Nagel and Michael E. Melich (Eds.), ISBN: 978-0-578-06694-3, 343, 2010.

[35] M. Swartz, Improved electrolytic reactor performance using pi-notch system operation and gold anodes, *Trans. Amer. Nucl. Assoc*., Nashville, Tenn Meeting, ISSN:0003-018X publisher LaGrange, Ill, 1998, pp. 78, 84–85.

[36] M.R. Swartz, Breakeven from LANR phusor device systems: relative limitations of thermal loss in feedback loop, in *Proc. 14th Int. Conf. Condensed Matter Nucl. Sci. and the 14th Int. Conf. Cold Fusion (ICCF-14)*, 10–15 August 2008, Washington, DC, David J. Nagel and Michael E. Melich (Eds.), ISBN: 978-0-578-06694-3, 689, 2010.

[37] S. Szpak and P.A. Mosier-Boss, On the behavior of the cathodically polarized Pd/D system: a response to Vigier's comments, *Phys. Lett*. A **22**1 (1996) 141–143.

[38] S. Szpak, P.A. Mosier-Boss, S.R. Scharber and J.J. Smith, Cyclic voltammetry of Pd+D codeposition, *J. Electroanal. Chem.* **380** (1995) 1–6.

[39] S. Szpak, P.A. Mosier-Boss and J.J. Smith, Deuterium uptake during Pd–D codeposition, *J. Electroanal. Chem*. **379** (1994) 121–127.

[40] S. Szpak, P.A. Mosier-Boss and F.E. Gordon, Further evidence of nuclear reactions in the pd/d lattice: emission of charged particles, *Naturwissenschaften* **94** (2007) 511–514.

[41] S. Szpak, P.A. Mosier-Boss, C. Young and F.E. Gordon, Evidence of nuclear reactions in the Pd lattice, *Naturwissenschaften* **92** (2005) 394–397.

[42] S. Szpak, P.A. Mosier-Boss, S.R. Scharber and J.J. Smith, Charging of the Pd/nH system: role of the interphase, *J. Electroanal. Chem*. **337** (1992) 147–163.

[43] S. Szpak, P.A. Mosier-Boss, M.H. Miles and M. Fleischmann, Thermal behavior of polarized pd/d electrodes prepared by co-deposition, *Thermochim. Acta* **410** (2004) 101–107.

[44] S. Szpak, P.A. Mosier-Boss and J.J. Smith, On the behavior of the cathodically polarized Pd/D system: search for emanating radiation, *Phys. Lett*. A **210** (1996) 382–390.

[45] S. Szpak, P.A. Mosier-Boss and J.J. Smith, On the behavior of pd deposited in the presence of evolving deuterium, *J. Electroanal. Chem.* **302** (1991) 255–260.

[46] S. Szpak, P.A. Mosier-Boss, R.D. Boss and J.J. Smith, On the behavior of the pd/d system: evidence for tritium production, *Fusion Techol.* **33** (1998) 38–51.

[47] S. Szpak et al., The effect of an external electric field on surface morphology of co-deposited Pd/D films, *J. Electroanal. Chem.* **580** (2005) 284–290.

[48] V. Violante, E. Castagna, C. Sibilia, S. Paoloni and F. Sarto, Analysis of Mi-hydride thin film after surface plasmons generation by laser technique, *Proc. 10th Int. Conf. on Cold Fusion*, Cambridge, MA, 2003.

[49] F.G. Will, K. Cedzynska and D.C. Linton, Tritium generation in palladium cathodes with high deuterium loading, *Trans. Fusion Technol.* **26** (1994) 209–213; Reproducible tritium generation in electrochemical cells employing palladium cathodes with high deuterium loading, *J. Electroanal. Chem* **360** (1993) 161–176.

[50] M. Swartz, Three physical regions of anomalous activity in deuterided palladium, *Infinite Energy* **14**(61) (2008) 19–31.

[51] M. Swartz and R., Optimal operating point manifolds in active, loaded palladium linked to three distinct physical regions, in *Proc. 14th Int. Conf. Condensed Matter Nucl. Sci. and the 14th Int. Conf. Cold Fusion (ICCF-14)*, 10–15 August 2008, Washington, DC, David J. Nagel and Michael E. Melich (Eds.), ISBN: 978-0-578-06694-3, 639, 2010.

[52] M. Swartz, Quasi-one-dimensional model of electrochemical loading of isotopic fuel into a metal, *Fusion Technol.* **22**(2) (1992) 296–300.

[53] M. Swartz, Isotopic fuel loading coupled to reactions at an electrode, *Fusion Technol.* **26**(4T) (1994) 74–77.

[54] M. Swartz, Optimal operating point characteristics of nickel light water experiments, *Proc. ICCF-7*, Vancouver, Canada, 1998, pp. 269.

[55] M. Swartz, Generality of optimal operating point behavior in low energy nuclear systems, *J. New Energy* **4**(2) (1999) 218–228.

[56] R.W. Bass and M.R. Swartz, Empirical system identification (ESID) and optimal control of lattice- assisted nuclear reactors, in *Proc. 14 Int. Conf. on Condensed Matter Nuclear Science*, DC, 2010.

[57]] M. Swartz and L.Forsley, Analysis of superwave-as-transitory-OOP-peak hypothesis, in *Proc. 14, Int. Conf. On Condensed Matter Nuclear Science*, DC, 2008.

[58] C.A. Hampel, *Rare Metal Handbook*, Reinhold, NY, 1954.
[59] M. Hansen and K. Anderko, *Constitution of Binary Alloys*, McGraw-Hill, NY, 1958.
[60] F.A. Cotton and G. Wilkinson, *Advanced Inorganic Chemistry*, Interscience, NY, 1972.
[61] L. F. Allard, E. Voelkl, D. S. Kalakkad and A. K. Datye, Electron holography reveals the internal structure of palladium nano-particles, *J. Materials Sci*. **29**(21) (1994) 5612–5614.
[62] M. Swartz, P.L. Hagelstein, G. Verner and K. Wright, Vacancy phase states in nickel cathodes, *Proc. of the Seventh International Conference on Cold Fusion* (ICCF-7), Vancouver, Canada, 1998, p. 137.
[63] Jan Marwan has improved the field by generating new methods of making additional vacancies with nanolipids and dyes.
[64] J. Meier J. Schiøtzb, P. Liub, 1.J.K. Nørskovb and U. Stimminga, Nano-scale effects in electrochemistry ?, *Chem. Phy. Lett*. **390**(4–6) (2004) 440–44.
[65] Chengcai Luo, Yuhong Zhang and Yanguang Wang, Palladiumnanoparticles in poly(ethyleneglycol): the efficient and recyclable catalyst for Heck reaction, *J. Mol. Catalysis A: Chemical* **229**(1–2) (2005) 7–12.
[66] Kensuke Naka, ? Hideaki Itoh and Yoshiki Chujo?, Self-organization of spherical aggregates of palladium nanoparticles with a cubic silsesquioxane, *Nano Lett.* **2** (11) (2002) 1183–1186.
[67] Anton Kiriy, SergiyMinko, ? Ganna Gorodyska, Manfred Stamm and Werner Jaeger, palladiumwire-shaped nanoparticles from single synthetic polycation molecules, *Nano Lett.* **2**(8) (2002) 881–885.
[68] Ping Lu, Toshiharu Teranishi, Kiyotaka Asakura, MikioMiyake and Naoki Toshima?, Polymer-protected Ni/Pd bimetallic nano-clusters: preparation, characterization and catalysis for hydrogenation of nitrobenzene, *J. Phys. Chem*. B, **103** (44) (1999) 9673–9682.
[69] P. G. Sandersa, J.R. Weertman and J.G. Barker, Structure of nanocrystalline palladium and copper studied by small angle neutron scattering, *J. Mater. Res*. **11** (1996) 12.
[70] Young-Min Chung and Hyun-Ku Rhee, *J. Catalysis Lett.* **85**(3–4) (2003) 159–164, Pt–Pd bimetallic nanoparticles encapsulated in dendrimer nanoreactor, Young-Min Chung1 and Hyun-Ku Rhee1, *J. Catalysis Lett*. **85**(3–4)(2003) 159-164.
[71] Karical R. Gopidas, James K. Whitesell, ? and Marye Anne Fox ?, synthesis, characterization and catalytic applications of a palladium–nanoparticle-cored dendrimer, *Nano Lett*. **3**(12) (2003) 1757–1760.
[72] D.R. Smith, J.B. Pendry and M.C.K.Wiltshire, Metamaterials and negative refractive index, *Science* (2004), sciencemag.org.
[73] Experimentalverification of backward-waveradiation from a negative refractive indexmetamaterial, *J. Appl. Phy.* (2002) [waves.utoronto.ca].
[74] D. Schurig, J.J. Mock, B.J. Justice and S.A. Cummer, Metamaterial electromagnetic cloak at microwave frequencies, *Science* (2006) sciencemag.org.
[75] G. Dolling, C. Enkrich, M. Wegener, C.M. Soukoulis, Simultaneous negative phase and group velocity of light in a meta material, *Science* (2006). sciencemag.org.
[76] G. Brodin, M. Marklund, L. Stenflo and P.K. Shukla, Anomalous reflection and excitation of surfacewaves in meta materials, *Phy. Lett*. A **367**(3) (2007) 233–236.
[77] E. Verney, B. Sauviac and C.R. Simovski, Isotropic metamaterial electromagnetic lens, *Phy. Lett*. A **315** (2004) 332.
[78] M. Marklund, P.K. Shukla, L. Stenflo and G. Brodin, Solitons and decoherence in left-handed metamaterials, *Phy. Lett*. A 341 (2005) 231–234.
[79] H. Chen, T-junction waveguide experiment to characterize left-handed properties of metamaterials, *J. Appl. Phy*. (2003). ceta-p6.mit.edu.
[80] J. Pendry et al. Defense advanced research projects agency, http://physics.ucsd.edu/∼drs, Air Force Office of Scientific Research (AFOSR).
[81] R.A. Shelby, D. R. Smith and S. Schultz, Experimental verification of a negative index of refraction, http://physics.ucsd.edu/∼drs, Appearing in the April 6, 2001 issue of Science.
[82] http://www.ee.duke.edu/Academics/Undergraduate/IndStudy03/ScottC2003.html, Towards Negative Index Material: Magnetic Response.
[83] J.E. Kielbasa, J. Liu, K.B. Ucer, D.L. Carroll and R.T., Sol-gel nanocomposites as metamaterials: preparation and optical measurements, *J. Materials Sci:. Materials Electronics* (2007).
[84] W. Wu, E. Kim, E. Ponizovskaya, Y. Liu, Z. Yu and N. Fang, Optical meta materials at near and Mid- IR range fabricated by nanoimprint lithography, *Appl. Phy. A: Materials Sci*. Processing 87 (2007) 143–150.

[85] W. Wu, Z. Yu, S.Y. Wang, R.S. Williams, Y. Liu and C. Sun, Mid-infrared metamaterials fabricated by nanoimprint lithography, Appl. Phy. Lett. (2007). link.aip.org... mat/pdf/0508/0508307.pdf; R. Marques, F.Medina and R. Rafii-El-Idrissi.
[86] D. Korobkin, Y.A, Urzhumov, B. Neuner III, C. Zorman, Mid-infrared metamaterial based on perforated Sic membrane: engineering optical response using Z.…, *Appl. Phy. A: Materials Sci. Processing* **88**(4) (2007) 605–609.
[87] C. Caloz and H.V. Nguyen, Novel broadband conventional-and dual-composite right/left-Handed (C/D-CRLH) meta materials, *Appl. Phy. A: Materials Sci. Processing* **87**(2) (2007) 309–316.
[88] Q. Wu, P. Pan, F.Y. Meng, L.W. Li and J. Wu, A novel flat lens horn antenna designed based on zero refraction principle of metamaterials, *Appl. Phy. A Materials Sci. Processing* (2007).
[89] M.W. Klein, C. Enkrich, M.Wegener and S. Linden, Second-harmonic generation frommagnetic metamaterials all 4 versions, *Science* (2006). sciencemag.org
[90] S. Linden, C. Enkrich, M. Wegener, J. Zhou and T. Koschny, Magnetic response of metamaterials at 100 THz, *Science* (2004). sciencemag.org.
[91] H.H. Uhlig, *Corrosion and Corrosion Control*, 2nd Edition, Wiley, Newyork, 1971.
[92] J.O'M Bockris and A.K.N. Reddy, *Modern Electrochemistry*, Plenum Press, 1970.
[93] A. Von Hippel, Dielectric Materials and Applications, MIT Press, Cambridge, 1954.
[94] J.R. Melcher, *Continuum Electromechanic*s, MIT Press, Cambridge, 1981.
[95] A. Von Hippel, D.B. Knoll and W.B. Westphal, Transfer of protons through pure ice 1 h single crystals, *J. Chem. Phys*. **54** (1971) 134, 145.
[96] M. Swartz, Dances with protons– ferroelectric inscriptions inwater/icerelevant tocold fusion and someenergy systems, *Infinite Energy* **44** (2002) 64–71.
[97] P.L. Hagelstein et al., A theoretical formulation for problems in condensed matternuclear science. in ICCF-14 Int. Conf. on Condensed Matter Nuclear Science, 2008, Washington, DC, P.L. Hagelstein and I. Chaudhary, Models Relevant to Excess Heat production in Fleischmann–Pons experiments, in *Low-Energy Nuclear Reactions Sourcebook*, J. Marwan and S. Krivit (Ed.), Oxford University Press, Oxford, 2008.
[98] M. Rabinowitz et al., Opposition and support for cold fusion, in *Fourth Int. Conf. on Cold Fusion*, Lahaina, Maui: Electric Power Research Institute, CA 94304, 1993.
[99] X.Z. Li et al., the precursor of cold fusion phenomenon in deuterium/solid systems. in anomalous nuclear effects in deuterium/solid systems, *AIP Conf. Proc.* 228, 1990, Brigham Young Univ., Provo, UT, American Institute of Physics, New York.
[100] A. Takahashi and N. Yabuuchi, Study on 4D/TSC condensation motion by non-linear Langevin equation, in Low-Energy Nuclear Reactions Sourcebook, J. Marwan and S. Krivit (Eds.), 2008, Oxford University Press, Oxford, A. Takahashi, Dynamic mechanism of TSC condensation motion, in *ICCF-14 Int. Conf. on Condensed Matter Nuclear Science*, 2008, Washington, DC.
[101] M. Swartz, Possible deuterium production from light water excess enthalpy experiments using nickel cathodes, *J. New Energy* **3** (1996) 68–80.
[102] M. Swartz, Phusons in nuclear reactions in solids, *Fusion Technol*. **31** (1997) 228–236.
[103] S.R. Chubb and T.A. Chubb, The role of hydrogen ion band states in cold fusion. *Trans. Fusion Technol.* **26**(4T) (1994) 414.
[104] T.A. Chubb and S.R. Chubb, Ion band states: what they are and how they affect cold fusion, in Cold Fusion Source Book, ibid. 75 (1994).
[105] M. Swartz, CatastrophicActive medium hypothesis o f cold fusion, Fourth Int. Conf. On Cold Fusion, sponsored by EPRI and the Office of Naval Research (1994); M. Swartz, Hydrogen redistribution by catastrophic desorption in select transition metals, *J. New Energy* **1**(4) (1977) 26–33.
[106] D.A. Papaconstantopoulos, B.M. Klein et al., Band structure and superconductivity of PdDx and PdHx, *Phy. Rev*. **17**(1) (1977) 141–150.
[107] E. Wicke and H. Brodowsky, Hy*drogen in Palladium and Palladium Alloys, Hydrogen in Metals II*, G. Alefield and J. Volkl (Eds.), Springer, Berlin, 1978.
[108] H. Teichler, Theory of hydrogen hopping dynamics including hydrogen-lattice correlations, *J. Less-Common Metals* **172–174** (1991) 548–556.
[109] B.M. Klein and R.E. Cohen, Anharmonicity and the inverse isotope effect in the palladium–hydrogen system, *Phys. Rev*. B

45 (1992) 21, 405.
[110] R.W. Bussard, Virtual-state internal nuclear fusion in metal lattices, *Fusion Technol.* **16** (1989) 231–236.
[111] T.C. Gibb, *Principles of Mossbauer Spectroscopy*, Chapman and Hall, London (1974).
[112] D.P.E. Dickson and F. Berry, *Mossbauer Spectroscopy*, Cambridge University Press, Cambridge, 1983.
[113] U. Gonser, *Mossbauer Spectroscopy*, Springer, NY, 1975.
[114] M. Swartz and G. Verner, Bremsstrahlung in hot and cold fusion, *J. New Energy* **3**(4) (1999) 90–101.
[115] M.R. Swartz, Excess heat and electrical characteristics of type B anode-plate high impedance phusor-type LANR devices, *J. Scientific Exploration*, American Chemical Society, Salt Lake City, UT, *J Scientific Exploration* **23**(4) (2009) 491–495.